Feeding and feedback in the inner kiloparsec of the active galaxy NGC 2110

Allan Schnorr-Müller,[1]* Thaisa Storchi-Bergmann,[1] Neil M. Nagar,[2]
Andrew Robinson,[3] Davide Lena,[3] Rogemar A. Riffel[4] and Guilherme S. Couto[1]

[1]*Instituto de Física, Universidade Federal do Rio Grande do Sul, 91501-970 Porto Alegre, RS, Brazil*
[2]*Astronomy Department, Universidad de Concepción, Casilla 160-C, Concepción, Chile*
[3]*Physics Department, Rochester Institute of Technology, Rochester, New York 14623, USA*
[4]*Departamento de Física, Centro de Ciências Naturais e Exatas, Universidade Federal de Santa Maria, 97105-900 Santa Maria, RS, Brazil*

ABSTRACT

We present two-dimensional gaseous kinematics of the inner $1.1 \times 1.6 \, \mathrm{kpc}^2$ of the Seyfert 2 galaxy NGC 2110, from optical spectra (5600–7000 Å) obtained with the Gemini Multi Object Spectrograph integral field spectrograph on the Gemini South telescope at a spatial resolution of $\approx$100 pc. Gas emission is observed over the whole field of view, with complex – and frequently double – emission-line profiles. We have identified four components in the emitting gas, according to their velocity dispersion (σ), which we refer to as: (1) warm gas disc ($\sigma = 100$–$220 \, \mathrm{km \, s}^{-1}$); (2) cold gas disc ($\sigma = 60$–$90 \, \mathrm{km \, s}^{-1}$); (3) nuclear component ($\sigma = 220$–$600 \, \mathrm{km \, s}^{-1}$) and (4) northern cloud ($\sigma = 60$–$80 \, \mathrm{km \, s}^{-1}$). Both the cold and warm disc components are dominated by rotation and have similar gas densities, but the cold gas disc has lower velocity dispersions and reaches higher rotation velocities. We attribute the warm gas disc to a thick gas layer which encompasses the cold disc as observed in some edge-on spiral galaxies. After subtraction of a rotation model from the cold disc velocity field, we observe excess blueshifts of $\approx$50 km s^{-1} in the far side of the galaxy (NE) as well as similar excess redshifts in the near side (SW). These residuals can be interpreted as due to nuclear inflow in the cold gas, with an estimated ionized gas mass inflow rate of $\phi \approx 2.2 \times 10^{-2} \, \mathrm{M_\odot \, yr^{-1}}$. We have also subtracted a rotating model from the warm disc velocity field and found excess blueshifts of $\approx$100 km s^{-1} to the SW of the nucleus and excess redshifts of $\approx$40 km s^{-1} to the NE, which we attribute to gas disturbed by an interaction with a nuclear spherical outflow. This nuclear outflow is the origin of the nuclear component observed within the inner 300 pc and it has a mass outflow rate of $0.9 \, \mathrm{M_\odot \, yr^{-1}}$. In a region between 1 and 4 arcsec north of the nucleus, which shows strong X-ray and [O III] $\lambda5007$ Å emission, we find a new low σ component of ionized gas which we attribute to a high latitude cloud photoionized by the nuclear source. The identification of the four distinct kinematic components has clarified the nature of the apparent asymmetry in the rotation curve of the galaxy pointed out in previous studies: it results from the dominance of different components to the south and north of the nucleus. We conclude that a comprehensive two-dimensional coverage of the kinematics and geometry of the nuclear gas around the active galactic nucleus is necessary to reveal the different processes at play, such as its feeding – via the cold inflowing gas – and the feedback, via the warm gas outflows.

Key words: galaxies: active – galaxies: individual: NGC 2110 – galaxies: kinematics and dynamics – galaxies: nuclei – galaxies: Seyfert.

1 INTRODUCTION

It is widely accepted that the radiation emitted by an active galactic nucleus (AGN) is a result of accretion on to the central supermassive black hole (hereafter SMBH). However, the exact nature of the

*E-mail: allan.schnorr@ufrgs.br

mechanisms responsible for transferring mass from galactic scales down to nuclear scales to feed the SMBH is still an open question. Theoretical studies and simulations (Shlosman, Begelman & Frank 1990; Emsellem, Goudfrooij & Ferruit 2003; Knapen 2005; Emsellem et al. 2006) have shown that non-axisymmetric potentials efficiently promote gas inflow towards the inner regions (Englmaier & Shlosman 2004). Imaging studies have revealed that structures such as small-scale discs or nuclear bars and associated spiral arms are frequently observed in the inner kiloparsec of active galaxies (Erwin & Sparke 1999; Pogge & Martini 2002; Laine et al. 2003). While bars can be effective in transporting gas into the inner few hundred parsecs, the fundamental problem of how gas gets from there down to the SMBH has remained unsolved. More recently, Simões Lopes et al. (2007) found that there is a marked difference in the dust and gas content of early-type active and non-active galaxies: while the first always have dusty structures, in the form of spiral and filaments at hundreds of parsecs scales, only 25 per cent of the non-active ones have such structures. This indicates that a reservoir of gas and dust is a necessary condition for the nuclear activity and also suggests that the dusty structures are tracers of feeding channels to the active galactic nuclei (hereafter AGN).

Previous results by our group in the optical includes the observation of inflow in the central region of NGC 1097 (Fathi et al. 2006), NGC 6951 (Storchi-Bergmann et al. 2007) and M81 (Schnorr Müller et al. 2011). In the particular case of M81, we could obtain not only the gas kinematics but also the stellar kinematics which was compared to the gaseous kinematics in order to isolate non-circular motions, instead of relying solely on the modelling of the gaseous kinematics as we did for NGC 1097 and NGC 6951. With the goal of looking for more cases of inward streaming motions, using all the methodologies we have developed in the previous papers, we began a project to map the gaseous kinematics around additional nearby AGN. After the observation of inflows in three low-ionization nuclear emission-line region galaxies, we decide to expand our sample to include also more luminous AGN in Seyfert galaxies in order to map the gas flows in a larger range of AGN luminosities.

In the current work, we present results obtained from integral field spectroscopic observations of the nuclear region of NGC 2110, a nearby (30.2 Mpc, from NED,[1] derived assuming a redshift of 0.007 789 and $H_0 = 73.0$) S0 galaxy harbouring a Seyfert 2 nucleus. NGC 2110 has been the subject of many studies at radio, near-infrared, optical, UV and X-ray wavelengths. It is classified as a narrow-line X-ray galaxy (Bradt et al. 1978) because of the strong X-ray emission. Radio observations show extended emission from a well-defined S-shaped radio jet, with an extent of ≈4 arcsec along the north–south direction (Ulvestad & Wilson 1983; Nagar et al. 1999), and strong nuclear variability (Mundell et al. 2009). Optical continuum images show a dusty circumnuclear disc with a spiral pattern and an S-shaped structure roughly parallel to the radio jet, the northern end of the 'S' being the site of [O III] and soft X-ray emission (Evans et al. 2006). Spectropolarimetric observations reported in Moran et al. (2007) revealed an extremely broad, double-peaked Hα emission line in the polarized flux spectrum, implying the existence of a disc-like hidden broad-line region. Integral field spectroscopy of the inner 10 arcsec (González Delgado et al. 2002; Ferruit et al. 2004) has shown that the gas kinematics at distances larger than 1 arcsec from the nucleus is asymmetric, the northern end of the S-shaped structure being related to the

asymmetry. In the inner 1 arcsec, the gas kinematics is complex with at least two components blueshifted relative to the systemic velocity, suggesting the presence of a nuclear outflow (González Delgado et al. 2002). This nuclear outflow was studied by Rosario et al. (2010) using *Hubble Space Telescope* (*HST*)-Space Telescope Imaging Spectrograph (STIS) data. They concluded that the outflow is oriented at a position angle (PA) offset by ≈40° from the PA of the main radio jet, suggesting the nuclear outflow skirts the radio jet instead of being cospatial to it. They also suggested that the S-shaped structure seen in the gas emission is ionized by the central AGN and not by shocks as the undisturbed kinematics of this region does not support the presence of the fast shock velocities needed to produce its high level of excitation.

This paper is organized as follows. In Section 2, we describe the observations and reductions. In Section 3, we present the procedures used for the analysis of the data and the subsequent results. In Section 4, we discuss our results and present estimates of the mass inflow rate and mass outflow rate and in Section 5, we present our conclusions.

2 OBSERVATIONS AND REDUCTIONS

The observations were obtained with the Integral Field Unit of the Gemini Multi Object Spectrograph (GMOS-IFU) at the Gemini South telescope on the night of 2011 January 28 (Gemini project GS-2010B-Q-19). The observations consisted of two adjacent IFU fields (covering 7×5 arcsec^2 each) resulting in a total angular coverage of 7×10 arcsec^2 around the nucleus with a sampling of 0.2 arcsec. Six exposures of 350 s were obtained for each field, slightly shifted and dithered in order to correct for detector defects after combination of the frames. The seeing during the observation was 0.6 arcsec, as measured from the full width at half-maximum (FWHM) of a spatial profile of the calibration standard. This corresponds to a spatial resolution at the galaxy of 95 pc.

The selected wavelength range was 5600–7000 Å, in order to cover the Hα+[N II] $\lambda\lambda 6548,6583$ and [S II] $\lambda\lambda 6716,6731$ emission lines, observed with the grating GMOS R400–G5325 (set to central wavelength of either λ 6500 Å or λ 6550 Å) at a spectral resolution of $R \approx 2000$ with 0.67 Å per pixel. Absolute flux calibration is expected to be accurate to ≈5 per cent, and the wavelength calibration is accurate to the order of 8 km s^{-1}.

The data reduction was performed using specific tasks developed for GMOS data in the GEMINI.GMOS package as well as generic tasks in IRAF.[2] The reduction process comprised bias subtraction, flat-fielding, trimming, wavelength calibration, sky subtraction, relative flux calibration, building of the data cubes at a sampling of 0.1 arcsec × 0.1 arcsec and finally the alignment and combination of the 12 data cubes.

3 RESULTS

In Fig. 1, we present in the upper-left panel the acquisition image of NGC 2110 and in the upper-right panel an image of the inner 22 arcsec × 22 arcsec of the galaxy obtained with the Wide Field Planetary Camera 2 (WFPC2) through the filter *F*606*W* aboard the *HST*. In the middle-left panel, we present a structure map of the WFPC2 *HST* image of NGC 2110 (see Simões Lopes et al. 2007), where nuclear structures delineated by dark (dusty) spirals

---

[1] The NASA/IPAC Extragalactic Database (NED) is operated by the Jet Propulsion Laboratory, California Institute of Technology, under contract with the National Aeronautics and Space Administration.

[2] IRAF is distributed by the National Optical Astronomy Observatories, which are operated by the Association of Universities for Research in Astronomy, Inc., under cooperative agreement with the National Science Foundation.
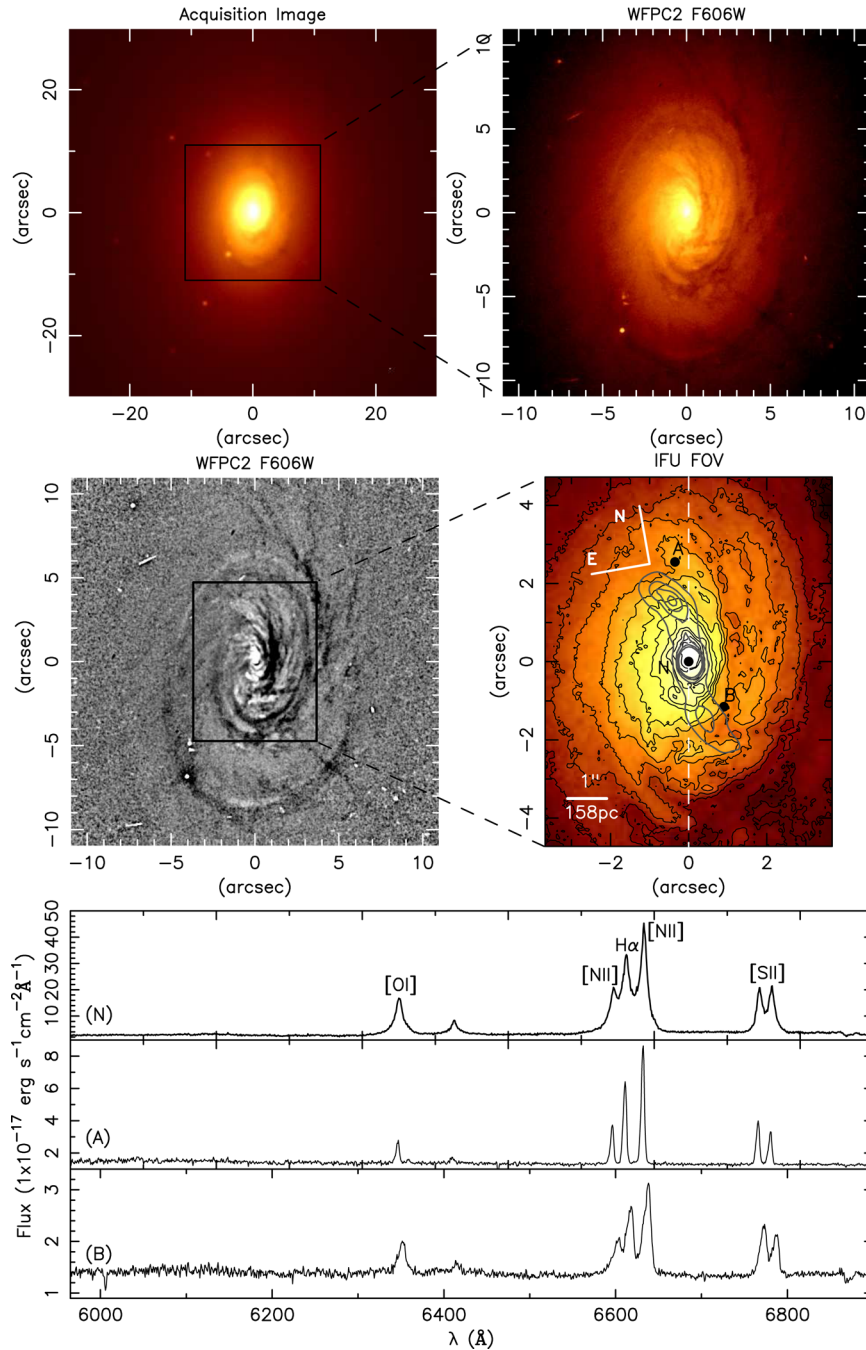
Figure 1. Top left: acquisition image. Top right: WFPC2 image of NGC 2110. Middle left: structure map of the galaxy, the rectangle shows the field of view of the IFU observation. Middle right: zoom in of the WFPC2 image showing the region covered by the IFU observations. Superposed contours trace the radio jet. The dashed white line indicates the position of the major axis of the galaxy (PA = 170° (Skrutskie et al. 2006)). Bottom: spectra corresponding to the regions marked as N, A and B in the IFU image.

can be seen. The rectangle shows the field of view (hereafter FOV) covered by the IFU observations. In the middle-right panel, we present a zoom in of the *HST* image showing the region covered by our observations. The superposed contours trace the radio jet. Note the presence of two bright spirals roughly (but not exactly) parallel to the radio jet. In the lower panel, we present three spectra of the galaxy corresponding to locations marked as A, B and N in the IFU image and extracted within apertures of 0.2 arcsec × 0.2 arcsec.

All the spectra are typical of Seyfert 2 galaxies, showing [O I] λλ 6300,6363, [N II] λλ6548,6583, Hα and [S II] λλ6717,6731

emission lines. The spectrum from location A shows very narrow emission lines, while those from the nucleus and from location B show broadened emission lines with blue wings. The nucleus has been assumed to be the location of the peak of the continuum emission.

3.1 Measurements

The gaseous centroid velocities, velocity dispersions and the emission-line fluxes were obtained by fitting Gaussians to the

[N II], Hα, [O I] and [S II] emission lines. Since the line profiles are often complex, we performed profile fits with a single Gaussian, two Gaussians and three Gaussians.

3.2 The single-Gaussian fit

In Fig. 2, we present a map of the signal-to-noise ratio of the [N II] λ6583 Å emission line. In Fig. 3, we present the resulting centroid velocity field, velocity dispersion and flux distribution of the [N II] emission line together with the [N II/Hα] ratio obtained from the single-Gaussian fit. A systemic velocity of 2229 km s^{-1} (see Section 4.1) was subtracted from the centroid velocity field. In order to limit the number of free parameters in our fit, we adopted the following physically motivated constraints.

(i) Flux$_{[N II] λ6583}$/Flux$_{[N II] λ6548}$ = 3;
(ii) The [N II] λ6583 and [N II] λ6548 lines have the same centroid velocity and FWHM.

The centroid velocity map displays a rotation pattern in which the N side of the galaxy is approaching and the S side is receding. Under the assumption that the spiral arms are trailing, it can be concluded that the near side of the galaxy is the W, and the far side is the E. The dust distribution (see the centre-left panel of Fig. 1) also suggests W is the near side of the galaxy. Although the centroid velocity maps display a rotation pattern, clear deviations from simple rotation are present, with the highest distortions observed to the west and north. Note that the rotational velocities observed north of the nucleus, specially in a region near the major axis, are lower than their southern counterpart. This asymmetry was first reported by Wilson & Baldwin (1985). More recently, González Delgado et al. (2002) and Ferruit et al. (2004) showed that the asymmetry is inherent to the gaseous velocity field, as the stellar velocity field is symmetric.

The velocity dispersion map shows high velocity dispersions (>200 km s^{-1}) in a region extending from 2 arcsec SW to 1.5 arcsec NE from the nucleus. Velocity dispersions of ≈180 km s^{-1} are observed in a region extending along the north–south direction located at ≈2 arcsec east of the nucleus. The lowest velocity dispersions
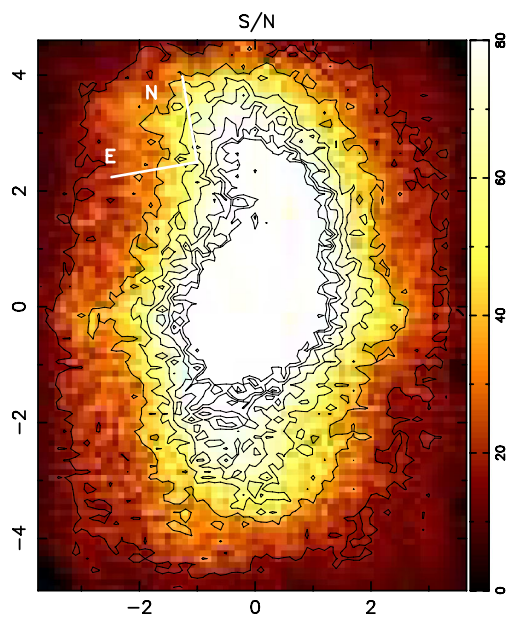
(<90 km s^{-1}) are observed in two spiral shaped regions one to the north and the other to the south of the nucleus. The northern low velocity dispersion region is cospatial to the region of low rotational velocity.

In the flux distribution, we observe two spiral arms approximately parallel to the radio and bending in a similar way. Both spirals are partly cospatial to the low velocity dispersion regions. The [N II/Hα] map shows that the southern low velocity dispersion region (where the southern spiral is located) shows [N II/Hα] < 1. A comparison with centroid velocity map shows that the northern spiral arm is cospatial to a region of low rotational velocities.

3.3 The two-Gaussian fit

As illustrated by spectra B and N in Fig. 1, the emission lines in the inner 1 arcsec have strong wings and a single-Gaussian fit, although providing a reliable estimate of the centroid velocity, does not provide reliable measurements of the velocity dispersion and flux distribution. González Delgado et al. (2002) and Ferruit et al. (2004) reported that they successfully fitted the emission line profiles of the inner 1 arcsec with two Gaussian components. We thus decided to perform a two-Gaussian fit to our data. As there is no easy way to determine the total extent of the region where a two-component fit is necessary, we performed the fit to the entire FOV. We used the continuity of the spectral properties of both components among neighbouring pixels as a criteria to decide if a given two-component fit was meaningful or not. In addition to the constraints applied to the single-Gaussian fit, we assumed that the Hα line has the same centroid velocity and FWHM as the [N II] lines.

We concluded that the presence of two components is required also beyond the inner 1 arcsec. Roughly, two components were necessary wherever the signal-to-noise ratio was larger than 40 (see Fig. 2). The only exception was a region extending from 3 arcsec south of the nucleus to the bottom of our FOV, where we observed two components even in regions with signal-to-noise ratio smaller than 40 (but larger than 20). Two components were also found for gas extending up to ≈2 arcsec in the east and west directions. In the top half, beyond the inner 1 arcsec, we only found two components along the northern spiral. The kinematics resulting from the two-component fit is complex, suggesting that in some locations even more than two components may be necessary in order to reproduce the gas kinematics. Based on the analysis of the centroid velocity and velocity dispersion maps, we concluded we have four components.

(i) A component we called warm gas disc because of its relatively high velocity dispersion, σ, between 100 and 220 km s^{-1}, and apparent rotation pattern of the centroid velocity.
(ii) A component we called the cold gas disc because of the low σ, between 60 and 90 km s^{-1}, and rotation pattern in the centroid velocity field.
(iii) A component present only within ≈1.5 arcsec from the nucleus, which we call the nuclear component, with σ in the range 220–600 km s^{-1}.
(iv) A component only present along the northern spiral arm, with σ in the range 60–80 km s^{-1} and centroid velocity close to the systemic velocity, which we called the northern cloud.

We present in Fig. 4 four characteristic spectra and the respective two-component fits. Spectrum N is typical of the inner 0.8 arcsec: the two components are very broad in this region (200 km s^{-1} for the warm gas disc and 600 km s^{-1} for the nuclear component) and observed in blueshift relative to the systemic velocity.

Figure 2. Map of the signal-to-noise ratio of the [N II] λ6583 Å emission line.
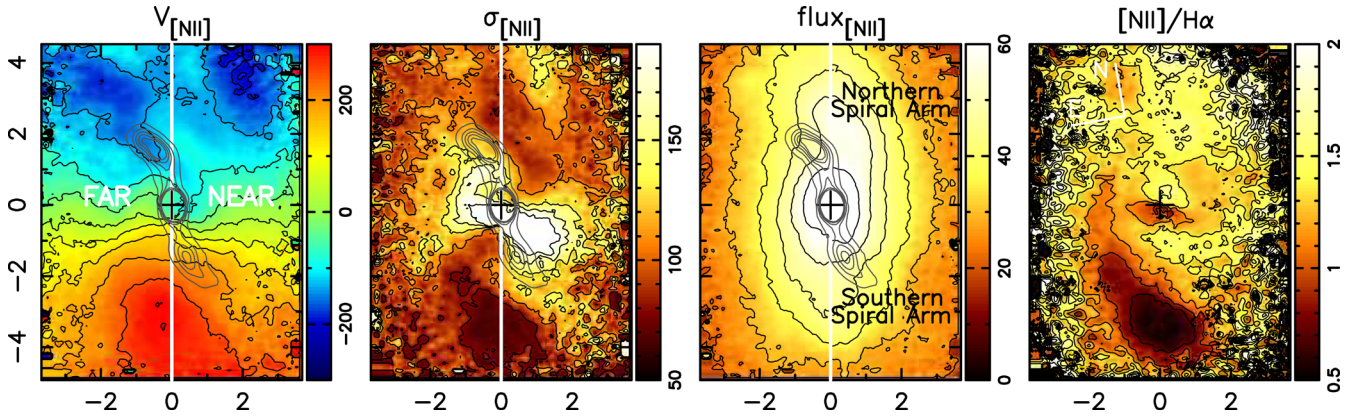
Figure 3. Centroid velocity (km s^{-1}), velocity dispersion (km s^{-1}), flux distributions (10^{-17} erg cm^{-2} s^{-1} per pixel) and [N II]/Hα line ratio resulting from the one-component fit.
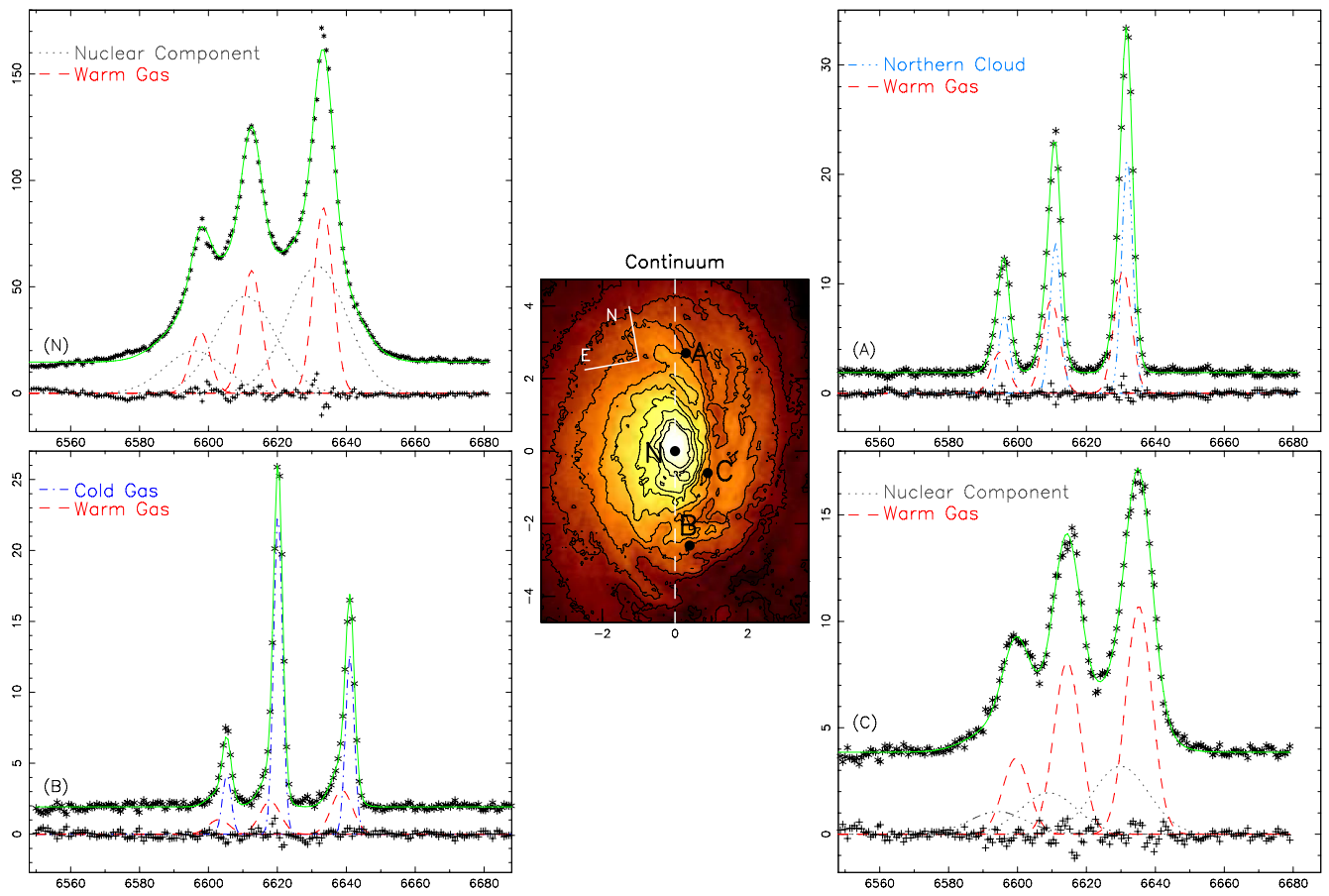
Figure 4. Illustration of the two-component fit for four different spectra.

Spectrum A is typical of the northern spiral: the emission lines have a broader base and a narrower top relative to a Gaussian profile. One of the components is very narrow ($\approx$60 km s^{-1}) with a centroid velocity close to the systemic velocity, attributed to the northern cloud. The other, the warm disc component, is broader ($\approx$100 km s^{-1}) with a centroid velocity of $\approx$−200 km s^{-1}. When we fitted this profile using only one component, the fitted Gaussian has essentially the low velocity dispersion of the northern cloud, but the centroid velocity is intermediate between the velocities of the northern cloud and the warm gas disc.

Spectrum B is typical of the region between 2 and 4 arcsec south of the nucleus: the lines are very narrow with a blue wing. The two-component fit yields one narrow ($\approx$60 km s^{-1}) and one relatively broad component ($\approx$140 km s^{-1}). The narrow component is rotating fast (with velocities of up to $\approx$300 km s^{-1}) with [N II]/Hα ratio values typical of H II regions ($<$0.5). We attribute this component to cold gas rotating in a thin disc in the plane of the galaxy. The broad component has a centroid velocity of 200 km s^{-1} and [N II]/Hα ratio values of the order of 1.2. We attribute this component to the warm gas disc. When fitting only one component to these lines, the

narrow component dominates, and the centroid velocities and velocity dispersions we obtain from the one-component fit in this region are essentially those of the cold gas disc. We note that although at first glance it may seem that the cold gas disc has stronger line emission than the warm gas disc, this is not true. The integrated fluxes from both components are comparable.

Spectrum C is typical of the high velocity dispersion region SW of the nucleus: a broad component (400 km s^{-1}), blueshifted in relation to the systemic velocity, which we attribute to the nuclear component, and a narrower (200 km s^{-1}) component, also blueshifted relative to the systemic velocity, which we attribute to the warm gas disc.

It is worth noting that although we cannot discard the possibility of three, or even four, components being present in a given spectrum, especially in the inner 1.5 arcsec, a three-Gaussian-component fit to our data does not give meaningful or stable results. While two of the components are essentially the same as the ones we obtained from the two-component fit, the parameters of the third component changed radically between neighbouring pixels and often resulted in non-physical profiles (amplitudes close to zero, extremely high velocities and velocity dispersions). We repeated the fit imposing upper and lower limits to the parameters, but this did not improve the stability of the parameters of the third Gaussian component.

We also tested the robustness of the two-component fits in the inner 1 arcsec. To do this, we varied the velocity dispersion of the narrow component from its best-fitting value and attempted a two-component fit. We noticed that if the velocity dispersion of the narrow component differs from its best-fitting value by more than 10 km s^{-1}, the fitted profile does not adequately reproduce either the wings or the peak of the observed profile. Thus, we conclude that the two-component fit is robust in the inner 1 arcsec.

Having identified the different kinematic components, the next step was to determine which one of these components exists in the regions in which one-component fits give better results than two-component fits, which we will refer to as the one component regions. Included in the one component regions are the top half of our FOV outside the northern spiral arm and the regions located beyond ≈2 arcsec to the east and west in the bottom half of the field. The centroid velocity field in the one component regions is clearly showing rotation, thus we could only attribute it to either the cold or warm gas disc. We then modelled the velocity fields of the cold and warm gas discs assuming a spherical potential model with pure circular motions (Bertola et al. 1991), subtracted each model from the centroid velocity field of the one component regions and used the minimization of the residuals as a criteria to decide which model reproduces it better. We found that in the one-component regions we are mapping the cold gas disc from the bottom of our FOV to ≈2 arcsec north of the nucleus, and mapping the warm gas disc in the remainder of the FOV.

3.4 Uncertainties in the measured quantities

To test the robustness of the fits and estimate the uncertainties in the quantities measured from each spectrum in our data cube, we performed Monte Carlo simulations in which Gaussian noise was added to the observed spectrum. For each spaxel, the noise added in each Monte Carlo iteration was randomly drawn from a Gaussian distribution whose dispersion was set to the expected Poissonian noise of that spaxel. One hundred iterations were performed and the estimated uncertainty in each parameter – line centre, line width and total flux in the line – was derived from the σ of the parame-

ter distributions yielded by the iterations. Uncertainties vary little among neighbouring pixels and become significant only when comparing regions with signal-to-noise ratios that differ by more than 20. Considering this, we divided our FOV into four different regions according to the signal-to-noise ratio of the [N II] λ6583 Å emission line (see Fig. 2) and then calculated the average uncertainties inside these regions. The average uncertainties are presented in Table 1.

3.5 The warm gas component

In Fig. 5, we present the gaseous kinematics, integrated flux distributions, line ratios and gas densities derived from the [N II] λ6583 Å, Hα, [O I] λ6300 Å and [S II] λ6716 Å emission lines.

The gaseous kinematics of the warm gas disc shows a rotation pattern with distortions in the inner 1 arcsec, where there is a strong contribution of the nuclear component. Comparing its velocity field to that of the single-Gaussian fit, the warm gas disc centroid velocity field is more symmetrical, with the velocities to the north of the nucleus being only slightly smaller (by ≈20 km s^{-1}) than those to the south. The velocity dispersion varies in the range 110–140 km s^{-1} over most of the FOV, reaching higher values (≈210 km s^{-1}) along a narrow strip running approximately from 1.5 arcsec east of the nucleus to 2 arcsec west, cospatial to observed distortions in the centroid velocity field.

The flux distribution is dominated by emission from the northern part of the FOV. The [N II]/Hα line ratio has values in the range of 1.2–2.0 in most of the FOV. The [O I]/Hα line ratio has values in the range 0.3–0.5, with lower values being observed at ≈2 arcsec north of the nucleus. The gas density map, obtained from the [S II] λλ6717/6731 line ratio assuming an electronic temperature of 10 000 K (Osterbrock 1989), shows values between 100 and 300 cm^{-3} over most of the FOV, reaching values larger than 400 in an almost unresolved knot at the nucleus.

3.6 The cold gas component

In Fig. 6, we present the gaseous kinematics, integrated flux distributions, line ratios and densities for the [N II] λ6583 Å, Hα, [O I] λ6300 Å and [S II] λ6716 Å emission lines.

The gaseous kinematics of the cold gas disc shows a rotation pattern similar to that of the warm gas disc component, but the velocities are higher. In a region extending from 2 arcsec south of the nucleus to the borders of the FOV we observe the lowest values of the velocity dispersion, between 60 and 70 km s^{-1}. From 2 arcsec to 0.6 arcsec south of the nucleus the velocity dispersion increases, reaching 80 km s^{-1}. At 1 arcsec west and east of the nucleus, the observed velocity dispersion reaches 90 km s^{-1}. The regions where the velocity dispersion is higher than 100 km s^{-1}, situated at >2 arcsec east and west, are the regions where we observed only one component.

A conspicuous feature of the flux distribution and line ratio maps is a southern spiral arm. At the region with lowest velocity dispersion, [N II]/Hα < 0.5 and [O I]/Hα < 0.2, values which are typical of [H II] regions. Surrounding this region, somewhat higher values are observed along an arm which extends to the east and north, passing to the east of the nucleus. These values are consistent with a combination of photoionization by the central source and young stars. The gas density map does not reveal any particular structure, the densities varying between 100 and 300 cm^{-3} over most of the FOV.

Table 1. Average uncertainties in velocity (km s⁻¹), velocity dispersion (km s⁻¹) and flux (per cent) for the different components and emission lines. Note that these numbers only reflect uncertainties in the process of fitting Gaussians to the spectra. Absolute uncertainties in these quantities are higher (see Section 2).

	SN > 80				80 > SN > 60			
	Cold disc	Warm disc	Nuclear Component	Northern Cloud	Cold disc	Warm disc	Nuclear Component	Northern Cloud
$\mathrm{Vel}_{[N\,II]}$	1	2	8	2	3	8	13	6
$\sigma_{[N\,II]}$	1	3	5	2	3	5	10	5
$\mathrm{Flux}_{[N\,II]}$	3	3	1	4	4	5	9	8
$\mathrm{Flux}_{H\alpha}$	1	5	2	4	1	6	12	8
$\mathrm{Vel}_{[O\,I]}$	2	2	3	5	4	6	7	9
$\sigma_{[O\,I]}$	3	4	6	3	4	8	12	8
$\mathrm{flux}_{[O\,I]}$	1	2	3	8	7	10	14	12
$\mathrm{Vel}_{[S\,II]}$	2	3	9	2	7	6	23	13
$\sigma_{[S\,II]}$	2	4	5	5	7	11	20	11
$\mathrm{Flux}_{[S\,II]}$	3	3	6	5	10	16	21	12
	60 > SN > 40				SN < 40			
	Cold disc	Warm disc	Nuclear Component	Northern Cloud	Cold disc	Warm disc	Nuclear Component	Northern Cloud
$\mathrm{Vel}_{[N\,II]}$	3	10	27	10	5	20	–	–
$\sigma_{[N\,II]}$	3	5	29	15	3	18	–	–
$\mathrm{Flux}_{[N\,II]}$	5	5	19	12	15	20	–	–
$\mathrm{Flux}_{H\alpha}$	2	7	25	13	20	20	–	–
$\mathrm{Vel}_{[O\,I]}$	15	16	–	–	22	–	–	–
$\sigma_{[O\,I]}$	17	19	–	–	24	–	–	–
$\mathrm{flux}_{[O\,I]}$	14	20	–	–	26	–	–	–
$\mathrm{Vel}_{[S\,II]}$	3	13	–	–	11	26	–	–
$\sigma_{[S\,II]}$	5	15	–	–	11	21	–	–
$\mathrm{Flux}_{[S\,II]}$	9	18	–	–	13	23	–	–

3.7 The nuclear component

Within ≈2 arcsec from the nucleus, the emission lines show a very broad component which we call the nuclear component. In Fig. 7, we present the corresponding gaseous kinematics, integrated flux distributions, line ratios and densities for the [N II] λ6583 Å, Hα, [O I] λ6300 Å and [S II] λ6716 Å emission lines.

The centroid velocity map shows blueshifted velocities in the near side of the galaxy, from 1 arcsec south to 2 arcsec north of the nucleus. Velocity dispersions of the order of 400 km s⁻¹ are observed east and west of the nucleus, cospatial with the highest velocities.

In the inner 1 arcsec the [N II]/Hα ratio is ≈1.5, increasing to ≈2 at larger radius. The density of the nuclear component reaches very high values, between 800 and 1000 cm⁻³, in a region extending from 1 arcsec south to 1.5 arcsec north, decreasing to ≈300 cm⁻³ elsewhere.

3.8 The northern cloud

We call this component the northern cloud because it shows distinct properties from those of the surrounding gas, as, for example, lower velocity dispersion and centroid velocities. It is cospatial to previously observed strong [O III]λ5007 and X-ray emission (Evans et al. 2006). In Fig. 8, we present its gaseous kinematics, integrated flux distributions, line ratios and densities derived from the [N II] λ6583 Å, Hα, [O I] λ6300 Å and [S II] λ6716 Å emission lines.

In spite of the small size of the cloud compared to our FOV, we observe a small velocity gradient which is consistent with rotational motion similar to that observed in the disc components, although with smaller velocity values. The velocity dispersion is small, being close to our velocity resolution, in the range 60–80 km s⁻¹.

The high [N II]/Hα ratios, between 1.4 and 1.8, are consistent with photoionization by the central source. The density of the cloud varies between 200 and 500 cm⁻³.

3.9 Channel maps

We have obtained channel maps along the [N II] λ6583 Å emission line profiles, which are shown in Fig. 9. They were built after the subtraction of the Hα emission line from the spectra. To test for any contamination due to artefacts resulting from a poor subtraction of the Hα line, we obtained channel maps along the [N II] λ6548 Å and compared it with the channel maps for the 6583 Å line. We found that both channel maps only differ in a region between 1 and 2 arcsec south of the nucleus in the panel corresponding to −606 km s⁻¹, where we only detect emission in the 6583 Å line. Thus, we attribute this emission to contamination and we do not consider it in our analysis.

Each panel presents the flux distribution in logarithmic units integrated within the velocity bin centred at the velocity shown in the top-right corner (relative to the systemic velocity of the galaxy). In the panels with velocities between 12 and −111 km s⁻¹, the strong emission from 1 to 4 arcsec north of the nucleus, close to the major axis, traces the northern cloud. Those velocities are consistent with what we obtain from the two-component fit. The velocity bins between −235 and −482 km s⁻¹ as well as between 136 and 445 km s⁻¹ are tracing rotation. Note that these panels are roughly symmetric. The emissions at the highest blueshifts and redshifts, 500–600 km s⁻¹, seem to trace the nuclear outflow in the inner 1 arcsec, as they are cospatial to the highest velocity dispersions in Fig. 7. We attribute the emissions detected between 1 and 2 arcsec north in the −544 and −606 km s⁻¹ panels and 1 and 2 arcsec south in the 507 and 569 km s⁻¹ panels to rotating gas.
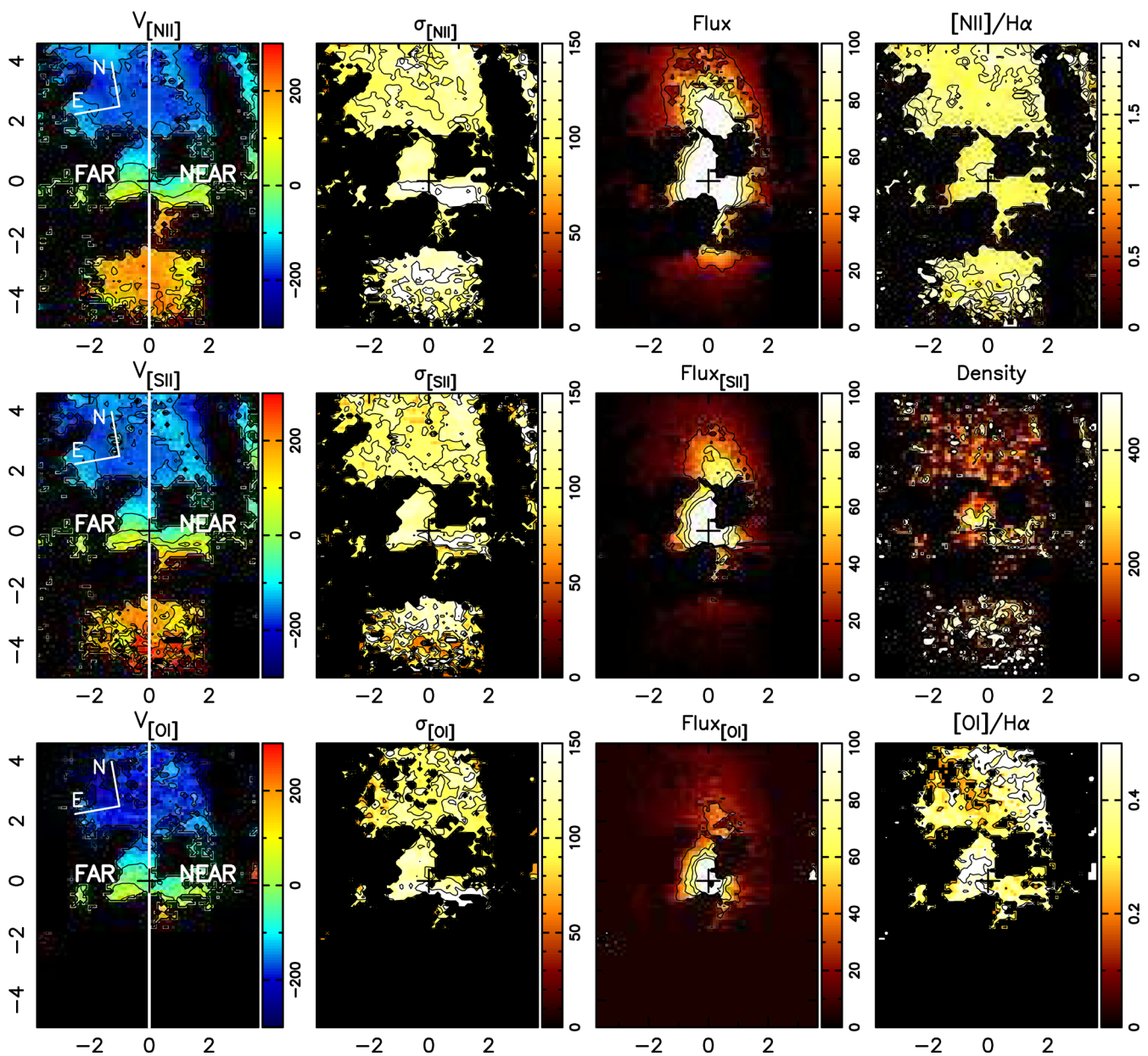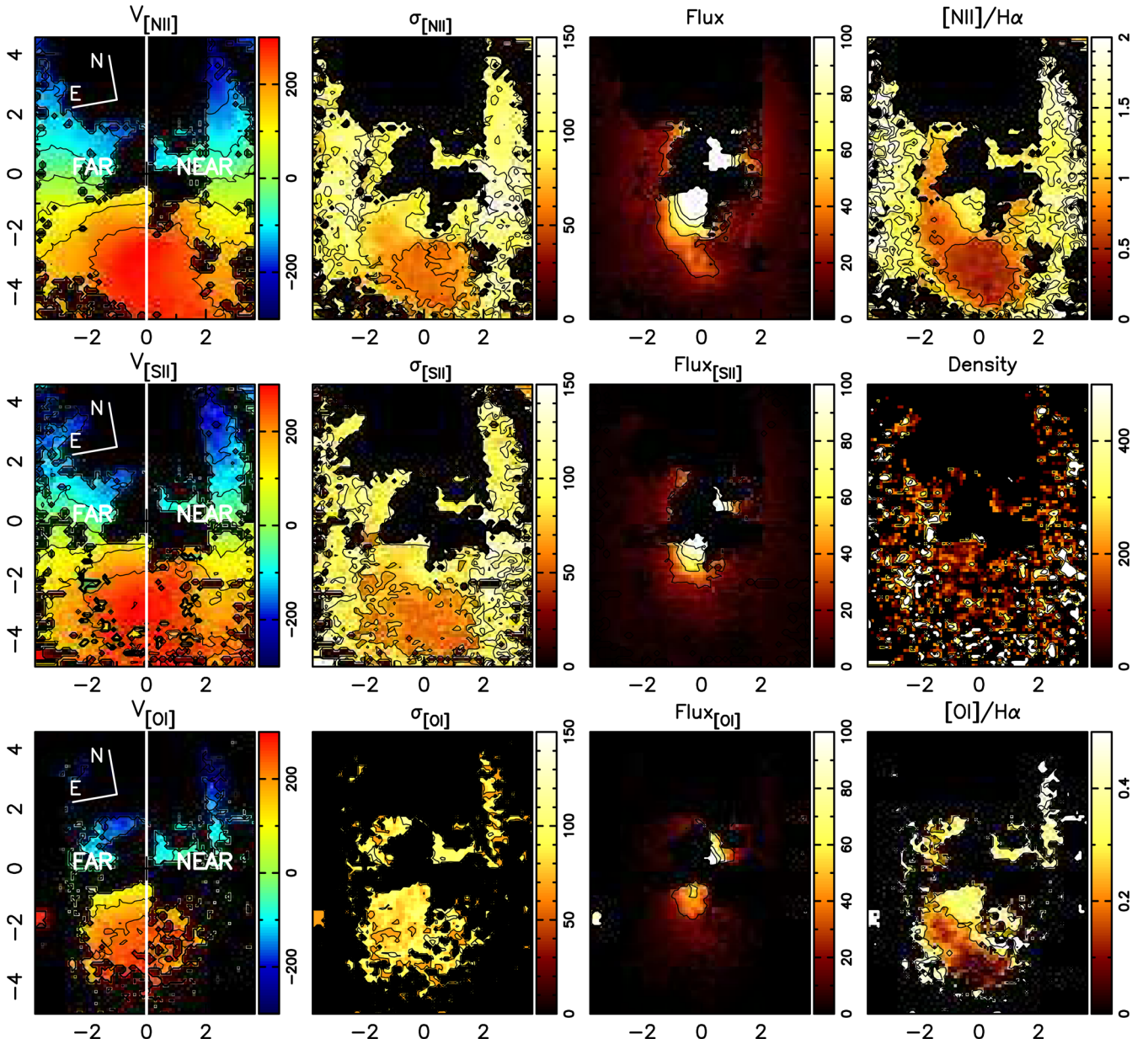
Figure 5. Centroid velocity (km s^{-1}), velocity dispersion (km s^{-1}), flux distributions (10^{-17} erg cm^{-2} s^{-1} per pixel), line ratios and density (cm^{-3}) of the warm gas disc.

4 DISCUSSION

As already mentioned, previous studies, in both optical and infrared wavelengths, reported an asymmetry in the gaseous velocity field of NGC 2110 (Wilson & Baldwin 1985; Storchi-Bergmann et al. 1999; Knop et al. 2001; González Delgado et al. 2002; Ferruit et al. 2004). This asymmetry was observed in the rotation curve along the major axis of the galaxy, which runs along north–south, with the southern part showing a larger velocity amplitude than the northern part, such that it appeared that the rotation centre is displaced to the south relative to the galaxy nucleus. González Delgado et al. (2002) have nevertheless shown that, although the gas velocity field was asymmetric, the stellar rotation was symmetric relative to the galaxy nucleus, with the velocity amplitude being lower than that of the gas. We also observe the asymmetry in the gas velocity field (see Fig. 3), as illustrated in Fig. 10, where we plot the velocity curve

along the major axis for the one-component fit, together with those for the different components. It can also be seen in Fig. 10 that the velocity field of the warm gas disc is practically symmetric relative to the galaxy nucleus (the velocities to the north are only $\approx$20 km s^{-1} larger than to the south, but this difference can be credited to uncertainties in the fit of the different components). Although we could not observe emission from the cold gas component along the major axis to the north (where the emission is completely dominated by the northern cloud and the warm gas), it is possible to observe it in the neighbouring regions, and in the next section we show that its velocity field is also symmetric relative to the nucleus. The apparent asymmetry in the one component kinematics is due to the fact that the gas emission is dominated by different components to the north and south of the nucleus: to the south the emission is dominated by the cold gas disc, which shows a larger velocity amplitude than

Figure 6. Centroid velocity (km s^{-1}), velocity dispersion (km s^{-1}), flux distributions (10^{-17} erg cm^{-2} s^{-1} per pixel), line ratios and density (cm^{-3}) of the cold gas disc.

that of the warm disc, while to the north the gas emission is due to both the warm component and the northern cloud (see spectrum A in Fig. 4); the measured velocities are thus intermediate between those of these two components, $\approx$100 km s^{-1} lower than the cold gas disc velocities. Separating the different kinematic components, there is no significant asymmetries in the velocity fields of both the cold and warm disc components, while the northern cloud is apparently at higher disc latitude, showing a smaller velocity than that corresponding to the rotation of the warm disc.

An inspection of Fig. 10 also illustrates why we cannot separate the cold and warm gas components in the inner 1 arcsec: rotation velocities for both components are similar in these scales. In the region where we observe the outflow, the flux seems to be dominated by the warm and nuclear components. Similarly, the northern cloud and the warm gas dominate the emission to the north.

4.1 Modelling of the velocity fields

In order to isolate non-circular motions in the cold and warm gas disc velocity fields, we modelled both independently assuming a spherical potential with pure circular motions, with the observed radial velocity at a position (R, ψ) in the plane of the sky (Bertola et al. 1991) given by

$$V = V_s + \frac{AR\cos(\psi - \psi_0)\sin(\theta)\cos^p\theta}{\{R^2[\sin^2(\psi - \psi_0) + \cos^2\theta\cos^2(\psi - \psi_0)] + c^2\cos^2\theta\}^{p/2}},$$

where θ is the inclination of the disc (with $\theta = 0$ for a face-on disc), ψ_0 is the PA of the line of nodes, V_s is the systemic velocity, R is the radius and A, c and p are parameters of the model. We assumed the kinematical centre to be cospatial with the peak of the continuum emission. In the case of the warm gas, we fixed the inclination
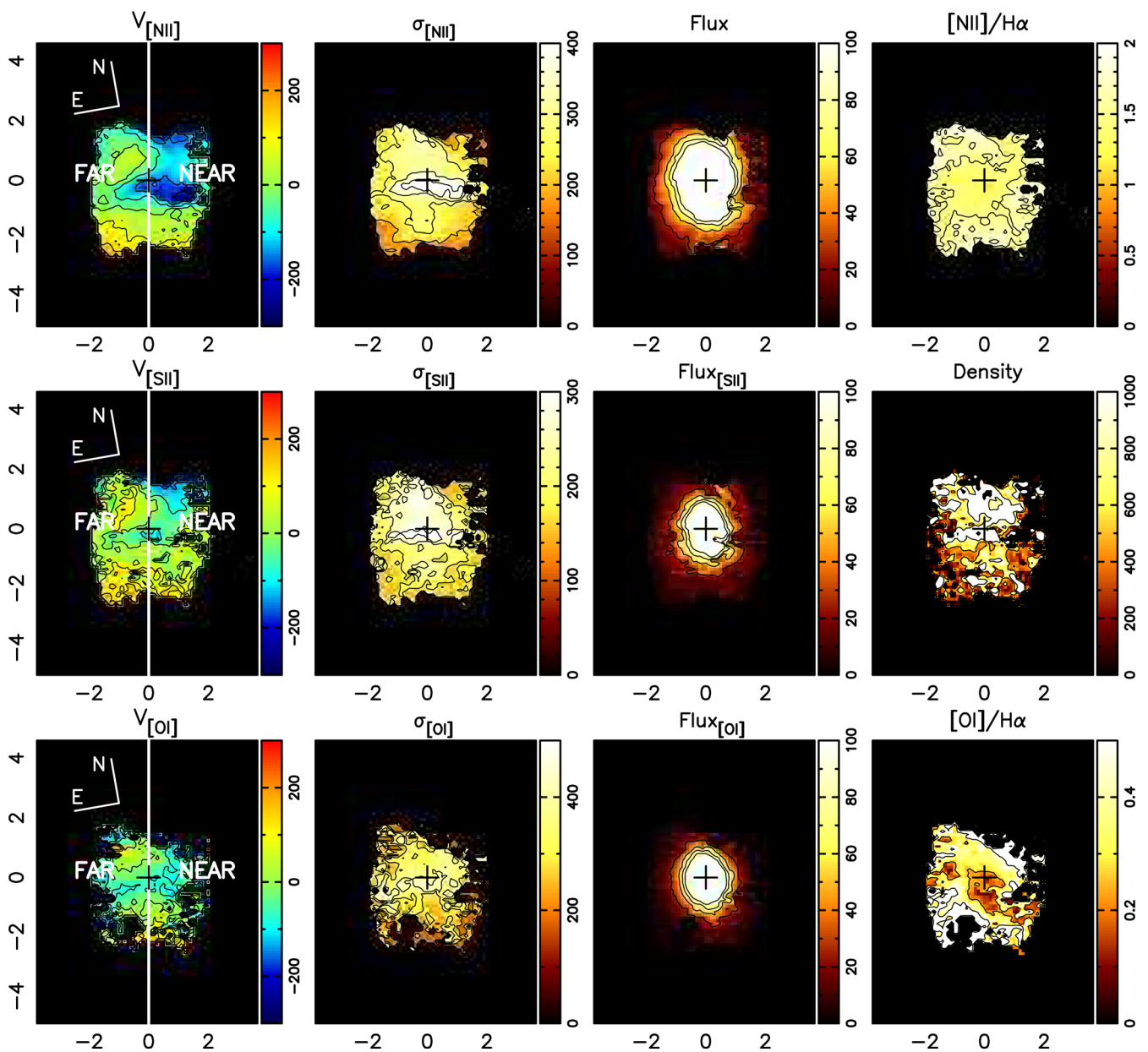
Figure 7. Centroid velocity (km s^{-1}), velocity dispersion (km s^{-1}), flux distributions (10^{-17} erg cm^{-2} s^{-1} per pixel), line ratios and density (cm^{-3}) of the nuclear component.

as 42° (González Delgado et al. 2002). For the cold gas, however, we left the inclination as a free parameter. The uncertainty in velocity resulting from the uncertainty in the wavelength calibration of 8 km s^{-1}, as well as the uncertainties derived from the Monte Carlo simulations (see Section 3.4) were taken into account in the fit.

For the fit of the cold gas disc centroid velocity field, the resulting parameters A, c and p are 1106 ± 2 km s^{-1}, 2.4 arcsec ± 0.1 and 1.4 ± 0.1, respectively. The systemic velocity corrected to the heliocentric reference frame is 2309 ± 10 km s^{-1} (taking into account errors in the Gaussian fitting process, the velocity field modelling and inaccuracies in the wavelength calibration), the PA of the major axis is $171° \pm 1$ and the inclination is $39° \pm 1$. The velocity field of this model is shown in Fig. 11. For the warm gas disc, the resulting parameters A, c and p are 377 ± 4 km s^{-1}, 1.3 arsec ± 0.1

and 1.2 ± 0.1, respectively. The systemic velocity corrected to the heliocentric reference frame is 2308 ± 11 km s^{-1} and the PA of the major axis is $169° \pm 1$. The velocity field for this model is shown in Fig. 12. Considering the good agreement of the systemic velocity obtained from both fits, we adopted 2309 ± 10 km s^{-1} as the systemic velocity of the galaxy.

4.2 Warm gas disc kinematics and excitation

The warm gas disc is characterized by velocity dispersions in the range 100–150 km s^{-1}. The [N II]/Hα line ratio ranges between 1.3 and 2 and the [O I]/Hα between 0.2 and 0.5, which is characteristic of AGN.

The centroid velocity field of the warm gas disc is dominated by rotation, as evidenced by the small residuals between its centroid
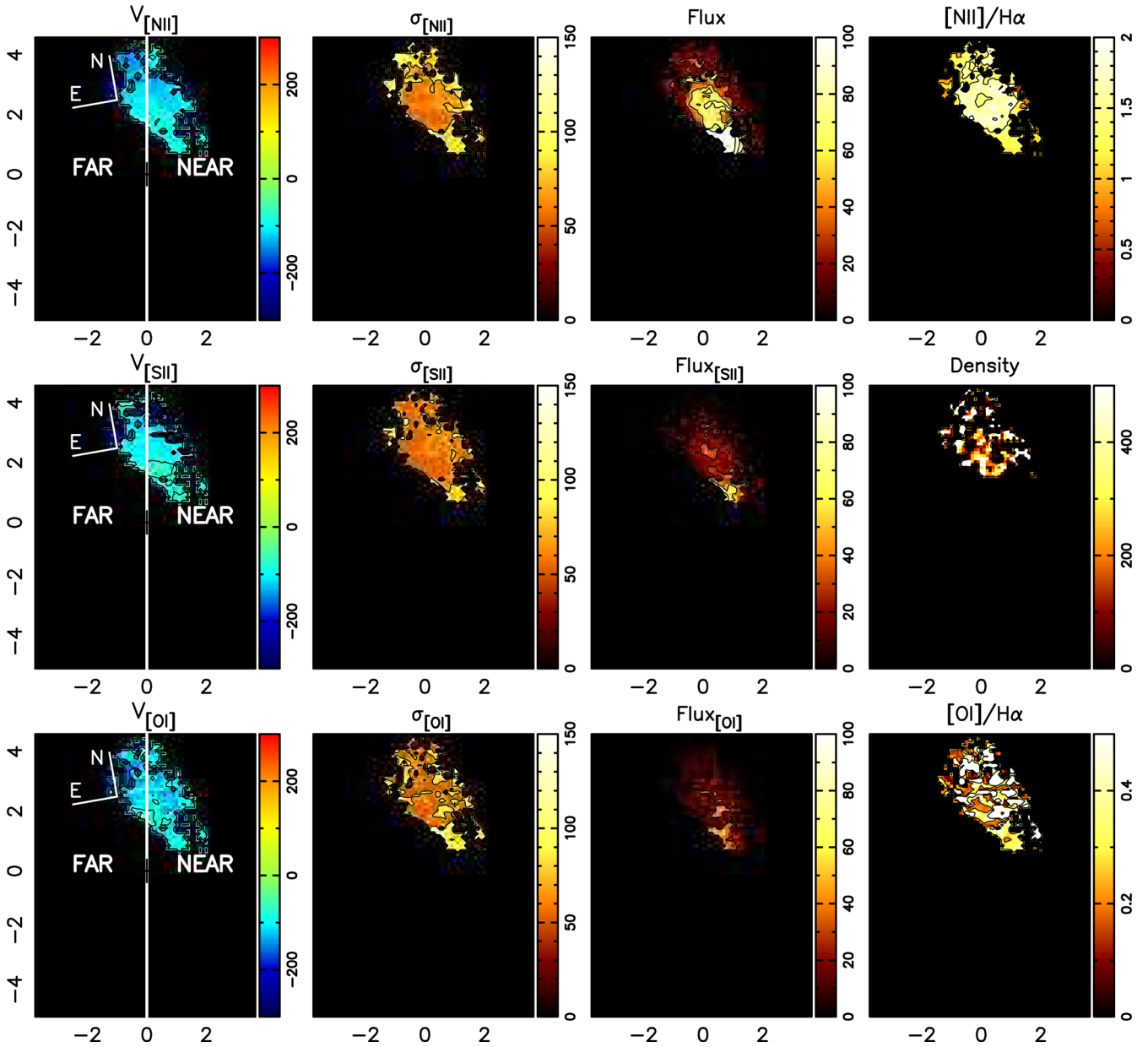
Figure 8. Centroid velocity (km s^{-1}), velocity dispersion (km s^{-1}), flux distributions (10^{-17} erg cm^{-2} s^{-1} per pixel), line ratios and density (cm^{-3}) of the northern cloud.

velocity field and the best-fitting circular model shown in Fig. 11. Residuals only exceed 30 km s^{-1} in three regions: (1) to the west of the nucleus, (2) in a region ≈2 arcsec south of the nucleus and (3) near the borders of the FOV. Most of the residuals are of the order of the uncertainties at these locations (see Table 1) and thus, although they can be due to non-circular motions, they can also be explained by uncertainties in the fit of the emission-line profiles. For example, the redshifted residuals (between 20–30 km s^{-1}) to the north of the nucleus are cospatial to the northern spiral arm, at a location we have found two components, the warm gas disc and the northern cloud. These residuals can thus be attributed to uncertainties in our two-component fit due to the small difference in velocity of these two components (about 60 km s^{-1}), and not necessarily to the presence of non-circular motions. The largest residuals are observed in blueshifts to the west of the nucleus, reaching 100 km s^{-1} and be-

ing cospatial to a region of high velocity dispersion (≈200 km s^{-1}). They are also cospatial to the highest centroid velocities and velocity dispersions observed in the nuclear component (see Fig. 7) and the highest velocity dispersions observed in the one-component fit (Fig. 3), and we thus suggest that these blueshifted residuals are due to gas in the disc disturbed by a nuclear outflow (see Section 4.6).

### 4.3 Cold gas disc kinematics and excitation

The cold disc is characterized by velocity dispersions lower than 100 km s^{-1}, reaching down to ≈60 km s^{-1} to the south of the nucleus. The region of low velocity dispersions in the south is delineated in the [N II]/Hα ratio map by values <0.5, which are typical of H II regions. We thus argue that the low velocity dispersion corresponds to a region which is now forming stars in an H II regions
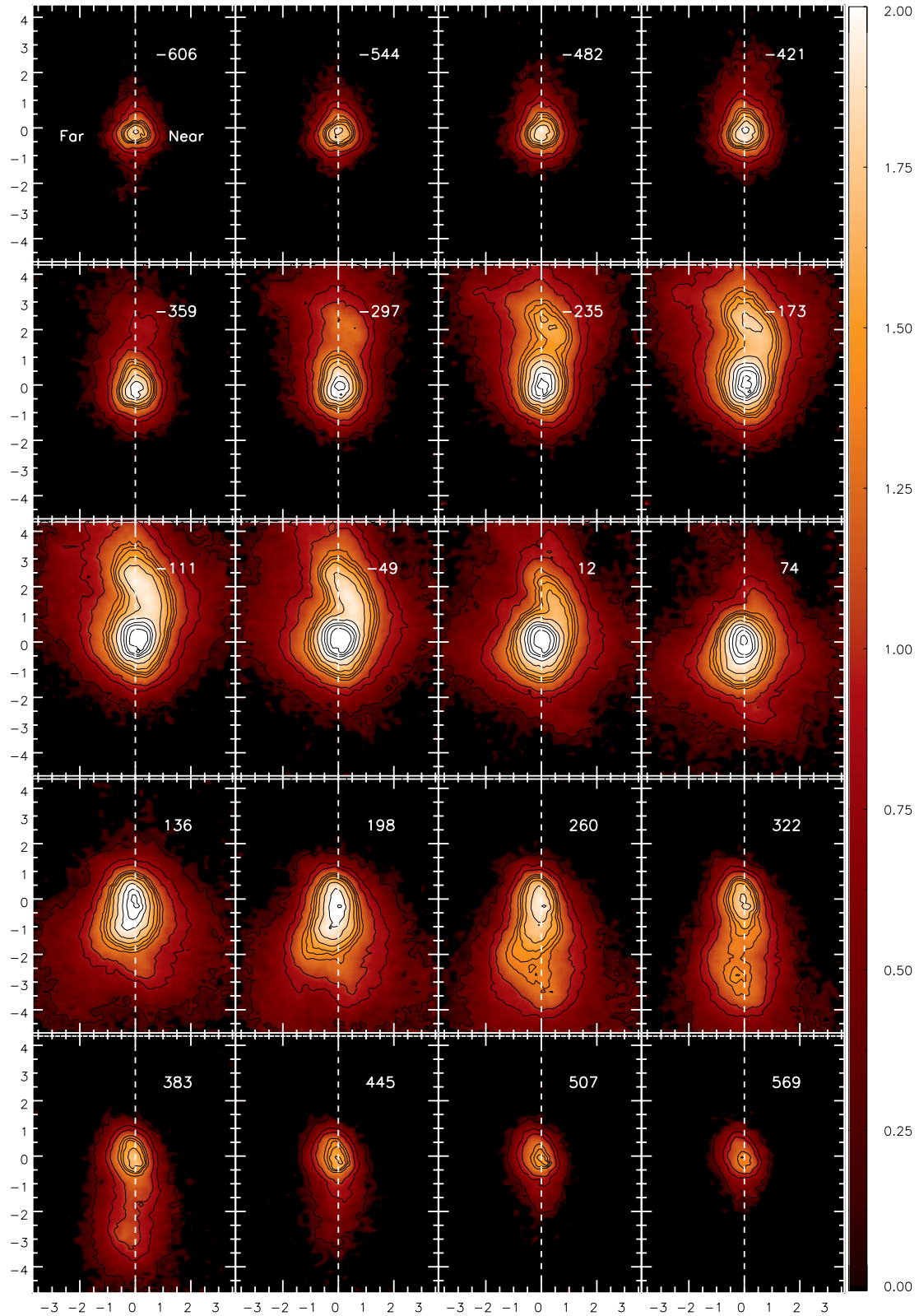
Figure 9. Channel maps for the [N II] emission line. The dashed white line marks the position of the photometric major axis.

complex. To the north of the complex and to the east of the nucleus, in the far side of the galaxy, there is a region of line-ratio values between 0.5 and 1. Although these values are not typical of H II regions, they are lower than those observed in the remaining field, which exceeds 1 everywhere. We thus conclude that in these regions we are observing the superposition of emission from gas photoionized by young stars in the galaxy plane and from gas ionized by the AGN.
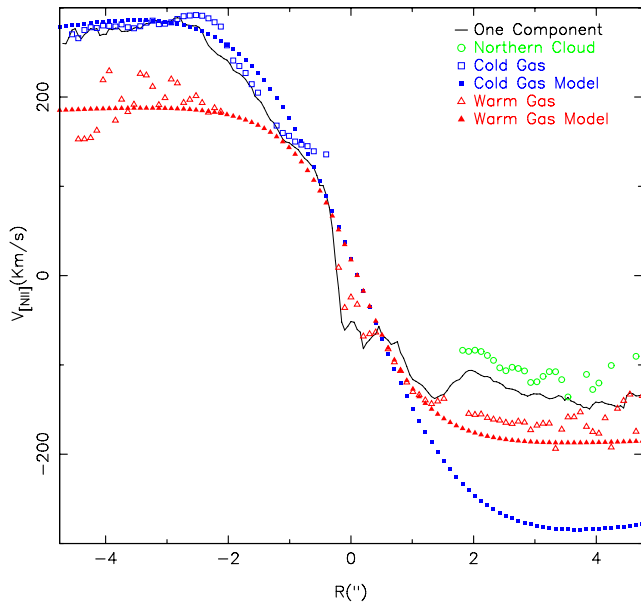
Figure 10. Comparison between the velocity curves along the major axis from the one-component fit, northern cloud, the cold and warm gas discs and the respective models.

The velocity field of the cold gas disc is also dominated by rotation. The residuals between the [N II] centroid velocity field and the circular model are shown in Fig. 12. They only exceed $30\,\mathrm{km\,s^{-1}}$ at ≈ 1.5 arcsec northeast and ≈ 1.5 arcsec southwest of

the nucleus, where they are of the order of $50\,\mathrm{km\,s^{-1}}$. Considering that this gas is in the plane and the residuals are in blueshift in the far side of the galaxy and in redshift in the near side, we argue that we are probably observing gas inflowing towards the nucleus of NGC 2110. Unfortunately, we cannot trace this inflow to smaller scales as the ionized gas emission in the inner 1 arcsec is dominated by the warm gas disc and the nuclear component, which do not allow us to isolate the cold disc component in this region.

### 4.4 Comparison with H$_2$ molecular gas kinematics

In order to investigate the possibility that we are observing inflowing gas in the cold disc kinematics, we compare our kinematics with that obtained from the H$_2\lambda 2.12\,\mu$m emission line from near-IR integral field spectroscopy using the Gemini Near-Infrared Integral Field Spectrometer (NIFS) instrument from Diniz et al. (in preparation), who kindly allowed the use of their results here. We present this comparison in Fig. 13, where we show the velocity field of the H$_2$ emitting gas and its residuals after the subtraction of the stellar velocity field as well as the residuals from the cold and warm gas discs after subtraction of the respective circular rotation model. A comparison between the H$_2$ and warm gas residual maps shows that the blueshifted residuals west of the nucleus are present in both maps, although restricted to a much smaller region in the H$_2$ map. Another feature of the H$_2$ residuals map is the presence of two spirals, showing blueshifts in the far side of the galaxy (NE) and redshifts in the near side (SW), part of which can also be found in our cold gas residual maps. We thus attribute these residuals
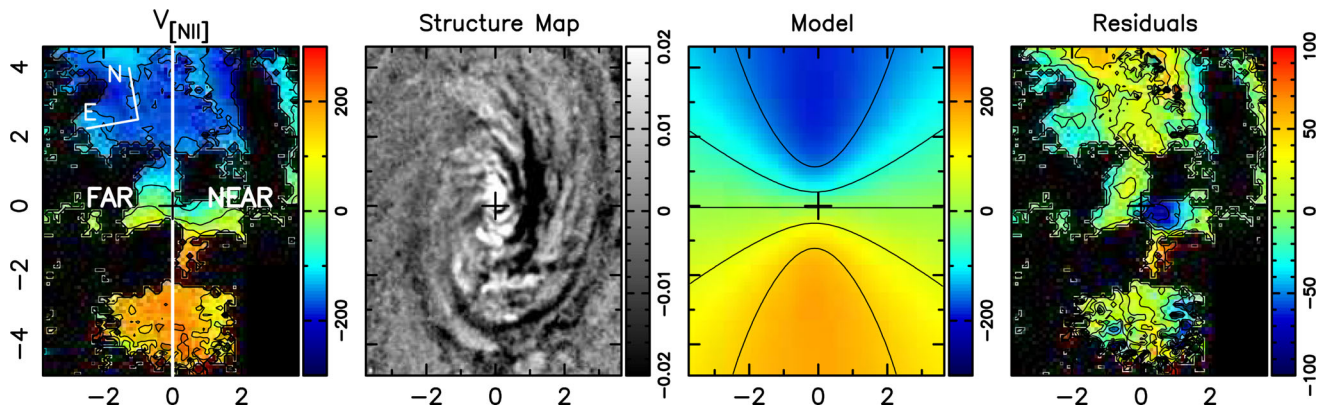
Figure 11. Centroid velocity, structure map, modelled velocity field and residuals for the warm gas disc.
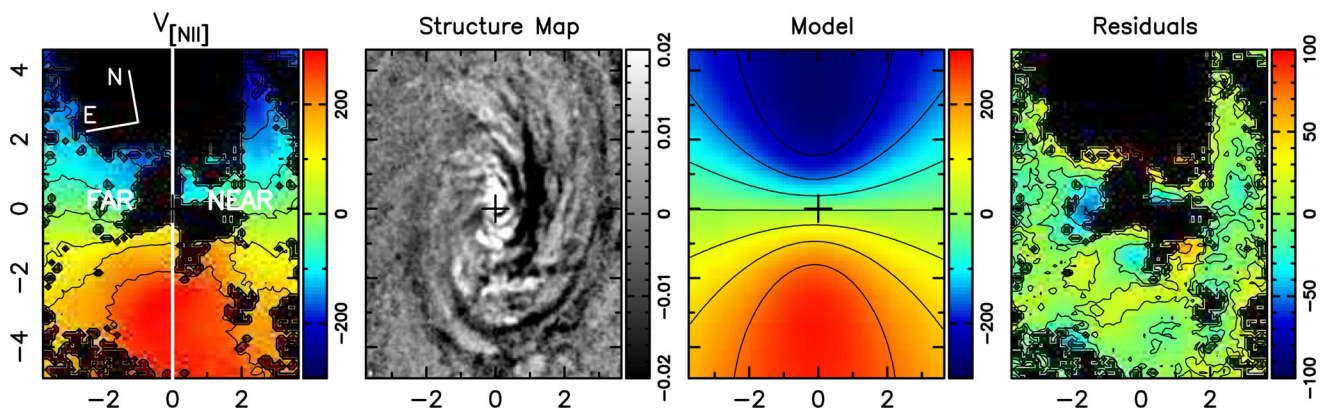
Figure 12. Centroid velocity, structure map, modelled velocity field and residuals for the cold gas disc.
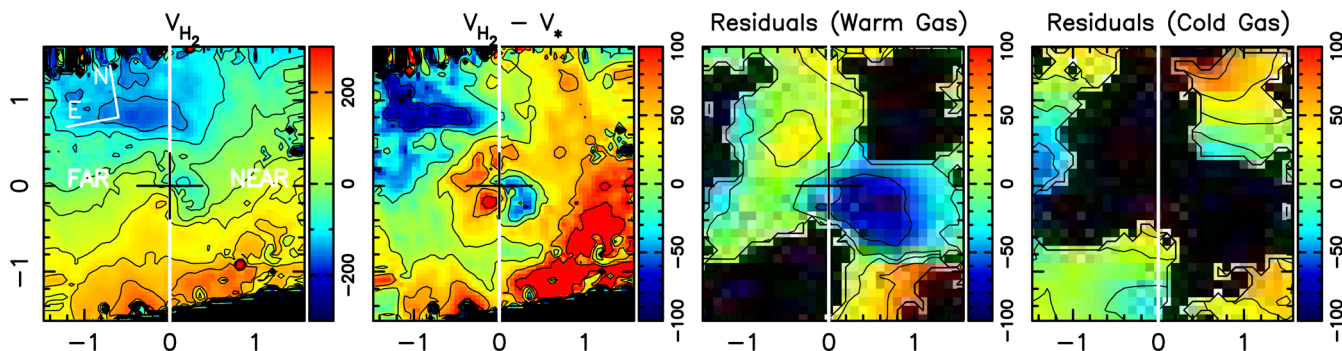
Figure 13. $H_2 2.12\,\mu m$ velocity field from Diniz et al. (in preparation) where we show the velocity field of the H_2 emitting gas and its residuals after the subtraction of the stellar velocity field as well as both the cold and warm gas discs after the subtraction of a circular rotation model.

to inflowing gas in the plane of the galaxy, in agreement with the interpretation of the H_2 residuals by Diniz et al.

4.5 The nature of the cold and warm gas discs

Observations of edge-on galaxies show that some of them, mostly late-type spirals with relatively high rates of star formation, have their discs encompassed by a thick layer of ionized gas, usually in the form of thick discs or haloes (Rand 1997; Rossa & Dettmar 2003; Rosado et al. 2013; Voigtländer et al. 2013). Regarding kinematics, these thick discs usually show signs of vertical gradients of rotation velocity or a lag in rotation velocity relative to the disc velocity (Heald et al. 2006; Kamphuis et al. 2007), as well as velocity dispersions higher than those characteristic of H II regions (Valdez-Gutiérrez et al. 2002). As the characteristics of the warm gas disc are consistent with this, we argue that the warm disc is a thick disc of ionized gas extending to somewhat higher galactic latitudes and encompassing the cold gas disc.

4.6 The nuclear component

The nuclear component, which is observed within the inner 2 arcsec radius is characterized by velocity dispersions in excess of $300\,km\,s^{-1}$. The FWHM map shows in particular a narrow feature along the galaxy minor axis extending by ≈ 1 arcsec to the east and ≈ 2 arcsec to the west in which the velocity dispersion reaches $500\,km\,s^{-1}$. To the south of the nucleus the velocity dispersions are smaller than to the north, $\approx 230\,km\,s^{-1}$, although still higher than the velocity dispersions associated with the cold and warm gas discs.

The centroid velocity kinematics shows, in the case of [N II] and Hα, blueshifts larger than $-200\,km\,s^{-1}$, which are observed along the high velocity dispersion feature, mainly to the west of the nucleus, with some blueshifts (of $\approx -100\,km\,s^{-1}$) also observed to the NW. Some redshifts are observed at ≈ 2 arcsec to the SE, while in the remainder of the field the centroid velocities are almost zero.

The blueshifts are observed mostly over the near side of the galaxy and can either be in the disc plane, or at high latitudes or extending from the disc to high latitudes and can thus only be in outflow. Our results are consistent with those found by González Delgado et al. (2002), who reported the presence of blueshifted gas at the nucleus of NGC 2110 as well as high velocity dispersions along the minor axis of the galaxy, which they interpreted as due to a nuclear outflow. More recently, Rosario et al. (2010) – using *HST*-STIS optical spectra – found the [O III]λ5007 emitting gas in the inner 0.2 arcsec to be blueshifted by $\approx 250\,km\,s^{-1}$ relative to

the systemic velocity and to have velocity dispersions larger than $1200\,km\,s^{-1}$. Although we do not observe velocity dispersions as high as those reported by Rosario et al. (2010), we do find high velocity dispersions at the nucleus, and the blueshifts are similar. Based on their long-slit data and narrow-band imaging, Rosario et al. (2010) proposed that the nuclear outflow is in a structure they call 'plume', which extends to only 0.5 arcsec from the nucleus at PA $= 150°$, making an angle of $\approx 30°$ with the galaxy major axis to the NW. Although we do not have enough spatial resolution to resolve the plume, we do find some blueshifts to the NW at the location of the plume and some redshifts to the SE, as described above, consistent with an orientation of the outflow in the NW-SE direction, as proposed by Rosario et al. (2010). On the other hand, the channel maps in Fig. 9 show that both the highest blueshifted and redshifted velocities are observed in a circular region of radius 2 arcsec and the velocity dispersion map for the one-component fit (Fig. 3) shows that the highest velocity dispersions are observed close to the minor axis, in a 'fan-shaped' structure oriented along NE-SW. The residuals between the warm gas velocity field and the circular rotating model in the inner 1 arcsec shown in Fig. 11, also show blueshifts to the SW and some redshifts (of $\approx 30\,km\,s^{-1}$) to the NE, which could be due to interaction of the nuclear outflow with the warm gas. The residuals between the H_2 velocity field and the stellar kinematics shown in Fig. 13 (Diniz et al., in preparation) also show blueshifts and redshifts approximately along the minor axis of the galaxy, supporting our results.

One possible interpretation for the nuclear component kinematics and spatial distribution is that of an expanding bubble originating in the galaxy nucleus. A spherically symmetric distribution of clouds ejected from the nucleus will be observed in each spectrum as the combination of gas expanding in different directions, thus resulting in a high velocity dispersion, as observed. The resulting flux distribution would be observed with a round shape, as is the case. In the case of the velocity map, an unobscured spherical outflow would show zero velocity. Dust in the plane of the galaxy, however, would cause obscuration mainly in the redshifted gas emission, which comes from behind the plane. Thus, the observed velocity field would be dominated by blueshifts. A large part of the nuclear component centroid velocity map does show velocities close to zero or slightly blueshifted ($<50\,km\,s^{-1}$), however regions with larger blueshifts are also observed. An inspection of the structure map in Fig. 12 shows that the largest blueshifts in the velocity map, mainly observed in the near side of the galaxy, are cospatial to dust lanes, in agreement with obscuration of the redshifted part of the outflow by dust in the plane of the galaxy. The channel maps in Fig. 9 support our interpretation of the nuclear component as a spherical outflow:

both the highest blueshifted and redshifted velocities ($\approx$500 km s^{-1}) are observed within the inner 300 pc, with the redshifted channels showing a slightly fainter emission, especially in the near side of the galaxy. In this scenario, we argue that the outflow seen in the warm gas is due to circumnuclear gas in the galaxy plane pushed by the spherical outflow as it moves away from the nucleus.

It is worth pointing out that, although nuclear outflows in nearby Seyfert 2 galaxies such as NGC 1068 (Das et al. 2006) and NGC 4151 (Storchi-Bergmann et al. 2010) have a conical morphology, this is not the case in NGC 2110. As discussed above, the nuclear outflow in NGC 2110 resembles instead spherically symmetric quasar-driven outflows. In a recent paper, this was shown to be the case even for type 2 quasars (Liu et al. 2013).

4.7 The northern cloud

Previous studies (González Delgado et al. 2002; Ferruit et al. 2004) already pointed out that the centroid velocities and velocity dispersions along the northern spiral (which is cospatial with the northern cloud) are lower than those of its surroundings. Also, as we already mentioned, [O III] and soft X-ray emission (Evans et al. 2006) are observed along the northern spiral. However, neither the origin of the [O III] and soft X-ray emission nor the origins of the lower rotational velocity and velocity dispersion have been explained. Rosario et al. (2010) argued that a direct interaction of the gaseous disc with the radio jet is unlikely, as they have concluded that the jet escapes the disc towards high latitudes very close to the nucleus (see the cartoon in fig. 7 of their paper). They also concluded that the gaseous kinematics along the northern spiral is incompatible with the presence of fast shocks (>500 km s^{-1}) necessary to produce its high level of excitation, concluding that it is photoionized by the central source. Taking all this into account, we argue that the [O III] emission and soft X-ray emission observed in the so-called 'northern' spiral, originate in fact in the northern cloud. The [N II]/Hα ratio values of the cloud are similar to those observed in the nuclear outflow, indicating that both regions are photoionized by the central source. We argue that, as in the case of the warm gas disc, the lower rotational velocities observed in the northern cloud compared to the surrounding gas implies that the northern cloud lies at higher latitudes.

4.8 Estimating the mass outflow rate

In the case of a spherically symmetric outflow, we can estimate the mass outflow rate from the ratio of the gas mass and dynamical time, M_g/t_d. From the channel maps in Fig. 9, we see that for velocities between 450 and 600 km s^{-1} the emission is dominated by outflowing gas. We thus adopt an outflow velocity of 525 km s^{-1}. Assuming a radius of 316 pc (2 arcsec) for the nuclear component, we obtain a dynamical time of $t_d \approx 6 \times 10^5$ yr. The gas mass is given by

$$M_g = N_e\, m_p\, V\, f,\tag{1}$$

where N_e is the electron density, m_p is the mass of the proton, V is the volume and f is the filling factor. The filling factor can be estimated from

$$L_{H\alpha} \sim f\, N_e^2\, j_{H\alpha}(T)\, V,\tag{2}$$

where $j_{H\alpha}(T) = 3.534 \times 10^{-25}$ erg cm^{-3} s^{-1} (Osterbrock 1989) and $L_{H\alpha}$ is the Hα luminosity emitted by a volume V. Substituting

equation (2) into equation (1) we have

$$M_g = \frac{m_p\, L_{H\alpha}}{N_e\, j_{H\alpha}(T)}.\tag{3}$$

From the Hα flux distribution and gas density of the nuclear component we obtain a gas mass of 5.5×10^5 M$_\odot$. The mass outflow rate is then $\approx$0.9 M$_\odot$ yr^{-1}.

4.9 Estimating the mass inflow rate

The cold gas kinematics suggests we are observing inflowing gas to the east and SW of the nucleus (see Fig. 12 and Section 4.3). We assume that both regions are in the disc plane and the total mass flowing through each of them is the same, a reasonable assumption considering that the densities, residual velocities and flux distributions of both regions are similar. The total gas mass inflow rate will thus be twice that through one region. As the uncertainties in the measurements corresponding to the region with blueshifted residuals are smaller, we have used the properties of this region in the calculation. The mass inflow rate through a cross-section of radius r can be obtained from

$$\dot{M}_{in} = N_e\, v\, \pi\, r^2\, m_p\, f,\tag{4}$$

where N_e is the electron density, v is the velocity of the inflowing gas, m_p is the mass of the proton, r is the cross-section radius and f is the filling factor. The filling factor can be estimated from equation (2). Substituting equation (2) into equation (4) and assuming the volume of the inflowing regions can be approximated by the volume of a cone with a radius r and height h, we have

$$\dot{M}_{in} = \frac{3\, m_p\, v\, L_{H\alpha}}{j_{H\alpha}(T)\, N_e\, h},\tag{5}$$

We adopt a distance to the nucleus of 1.7 arcsec. At this distance, the line-of-sight component of the average inflow velocity is 50 km s^{-1} (Fig. 12), corresponding to a velocity in the plane of the galaxy of $v = 79$ km s^{-1}. The average electron density is 200 cm^{-3} (see Fig. 6). The total Hα flux inside the region is 3.0×10^{-14} erg cm^{-2} s^{-1}. Adopting a distance to the galaxy of 30.2 Mpc, we obtain $L_{H\alpha} = 3.2 \times 10^{39}$ erg s^{-1}. After substituting these quantities into equation (5), we obtain a total inflow rate of $\phi \approx 2.3 \times 10^{-2}$ M$_\odot$ yr^{-1}. This value is two orders of magnitude lower than our estimate of the mass outflow rate, but we are only observing ionized gas, which is probably only the 'hot skin' of a larger inflow dominated by neutral and molecular gas.

We can now compare the mass inflow and outflow rates in the nuclear region to the mass accretion rate necessary to produce the luminosity of the Seyfert nucleus of NGC 2110, calculated as follows:

$$\dot{m} = \frac{L_{bol}}{c^2\eta}$$

with $\eta \approx 0.1$ (Frank, King & Raine 2002) (as usually adopted for Seyfert galaxies). The nuclear luminosity can be estimated from the X-ray luminosity of $L_X = 2.9 \times 10^{42}$ erg s^{-1} (Pellegrini 2010), using the approximation that the bolometric luminosity is $L_B \approx 10 L_X$. We use these values to derive an accretion rate of $\dot{m} = 5 \times 10^{-3}$ M$_\odot$ yr^{-1}.

The nuclear accretion rate is four times smaller than the mass inflow rate, what shows that much more gas is flowing in than the necessary to feed the AGN (considering in addition that the gas inflow is probably dominated by neutral and molecular gas, as pointed out above).

The nuclear accretion rate is two orders of magnitude smaller than the outflow mass rate, a ratio comparable to those observed for other Seyfert galaxies (Riffel & Storchi-Bergmann 2011). This implies that most of the outflowing gas does not originate in the AGN, but in the surrounding interstellar medium, which is pushed away from the nucleus by an AGN outflow.

5 CONCLUSIONS

We have measured the gaseous kinematics in the inner $1.1 \times 1.6 \, \text{kpc}^2$ of the Seyfert 2 galaxy NGC 2110, from optical spectra obtained with the GMOS integral field spectrograph on the Gemini South telescope at a spatial resolution of $\approx 100 \, \text{pc}$. The main results of this paper are as follows.

(i) The gaseous kinematics is complex and in most of the FOV two components are needed to adequately fit the emission lines. Considering the complete FOV, we identify four distinct kinematic components which we call warm gas disc, cold gas disc, nuclear component and northern cloud.

(ii) The cold gas disc has a low σ (60–90 km s^{-1}) and is rotating with velocities of the order of 300 km s^{-1}. A large H II region – characterized by [N II]/Hα ratios ≤ 0.5 – is observed in this component. After subtraction of a rotation model, excess blueshifts to the NE (the far side of the galaxy) and redshifts to the SW (the near side of the galaxy) of ≈ 50 km s^{-1} can be interpreted as inflows towards the nucleus.

(iii) The warm gas disc has $100 \leq \sigma \leq 220$ km s^{-1} and rotates ≈ 100 km s^{-1} slower than the cold disc. We interpret this component as a thick disc of gas extending to higher galactic latitudes and encompassing the cold disc, similar to what is observed in edge-on spiral galaxies. After subtraction of a rotation model, we observe excess blueshifts to the SW of the nucleus and excess redshifts to the NE. We suggest these residuals are due to gas in the disc disturbed by an interaction with the nuclear component. The emission-line ratios are typical of AGN, and we thus conclude that this gas is ionized by the active nucleus;

(iv) The nuclear component has a very high σ, between 220 and 600 km s^{-1} and no rotation. We interpret this component as an expanding bubble of gas, a scaled down form of the spherical nuclear outflows characteristic of quasars.

(v) The northern cloud has a much lower velocity dispersion than the surrounding gas, with $60 \leq \sigma \leq 80$ km s^{-1}, shows also a lower rotation velocity than the surrounding gas and its location is the site of X-ray emission previously observed 'along the northern spiral'. We interpret this component as due to a gas not in the plane but in a cloud at high latitudes, being ionized by the AGN (as the surrounding gas in the plane);

(vi) In previous observations, this galaxy was found to present an asymmetric rotation curve in the emitting gas. We show that the apparent asymmetry is due to the fact that different locations are dominated (in flux) by distinct kinematic components. When separated, each component, such as the cold and warm discs, have symmetric rotation curves. The presence of the northern cloud and nuclear component also contribute to the apparent asymmetry of the gas velocity field.

(vii) From the measured velocities, fluxes and density of the outflowing gas, we estimate a mass outflow rate of $\dot{M}_{\text{out}} \approx 0.9 \, \text{M}_\odot \, \text{yr}^{-1}$. This outflow rate is two orders of magnitude larger than the accretion rate to the AGN, implying that the measured outflow cannot originate in the AGN but instead is due to mass-loading of a nuclear outflow by circumnuclear gas;

(viii) From the measured gas velocities and fluxes of the inflowing gas – seen in the cold disc component – we estimate an ionized gas mass inflow rate of $\phi \approx 2.2 \times 10^{-2} \, \text{M}_\odot \, \text{yr}^{-1}$. We argue that this may be only the 'hot skin' of a larger gas flow dominated by neutral and molecular gas. The gas inflow rate is thus at least four times larger than the AGN accretion rate, implying that more gas is migrating to the centre of the galaxy than the necessary to feed the AGN.

With our observations, we are thus resolving both the feeding of the AGN – via the cold inflowing gas– and its feedback – via the nuclear outflow in the nuclear component and warm disc – around the active nucleus of NGC 2110.

REFERENCES

Bertola F., Bettoni D., Danziger J., Sadler E., Sparke L., de Zeeuw T., 1991, ApJ, 373, 369
Bradt H. V., Burke B. F., Canizares C. R., Greenfield P. E., Kelley R. L., McClintock J. E., van Paradijs J., Koski A. T., 1978, ApJ, 226, L111
Das V., Crenshaw D. M., Kraemer S. B., Deo R. P., 2006, AJ, 132, 620
Emsellem E., Goudfrooij P., Ferruit P., 2003, MNRAS, 345, 1297
Emsellem E., Fathi K., Wozniak H., Ferruit P., Mundell C. G., Schinnerer E., 2006, MNRAS, 365, 367
Englmaier P., Shlosman I., 2004, ApJ, 617, L115
Erwin P., Sparke L. S., 1999, in Merritt D. R., Valluri M., Sellwood J. A., eds, ASP Conf. Ser. Vol. 182, Galaxy Dynamics. Astron. Soc. Pac., San Francisco, p. 243
Evans D. A., Lee J. C., Kamenetska M., Gallagher S. C., Kraft R. P., Hardcastle M. J., Weaver K. A., 2006, ApJ, 653, 1121
Fathi K., Storchi-Bergmann T., Riffel R. A., Winge C., Axon D. J., Robinson A., Capetti A., Marconi A., 2006, ApJ, 641, L25
Ferruit P., Mundell C. G., Nagar N. M., Emsellem E., Pécontal E., Wilson A. S., Schinnerer E., 2004, MNRAS, 352, 1180
Frank J., King A., Raine D. J., 2002, in Frank J., King A., Raine D., eds, Accretion Power in Astrophysics, 3rd edn. Cambridge Univ. Press, Cambridge, p. 398 (ISBN 0521620538)
González Delgado R. M., Arribas S., Pérez E., Heckman T., 2002, ApJ, 579, 188
Heald G. H., Rand R. J., Benjamin R. A., Collins J. A., Bland-Hawthorn J., 2006, ApJ, 636, 181
Kamphuis P., Peletier R. F., Dettmar R.-J., van der Hulst J. M., van der Kruit P. C., Allen R. J., 2007, A&A, 468, 951
Knapen J. H., 2005, Ap&SS, 295, 85
Knop R. A., Armus L., Matthews K., Murphy T. W., Soifer B. T., 2001, AJ, 122, 764

Laine S., van der Marel R. P., Rossa J., Hibbard J. E., Mihos J. C., Böker T., Zabludoff A. I., 2003, AJ, 126, 2717

Liu G., Zakamska N. L., Greene J. E., Nesvadba N. P. H., Liu X., 2013, MNRAS, preprint (arXiv:e-prints)

Moran E. C., Barth A. J., Eracleous M., Kay L. E., 2007, ApJ, 668, L31

Mundell C. G., Ferruit P., Nagar N., Wilson A. S., 2009, ApJ, 703, 802

Nagar N. M., Wilson A. S., Mulchaey J. S., Gallimore J. F., 1999, ApJS, 120, 209

Osterbrock D. E., 1989, Astrophysics of Gaseous Nebulae and Active Galactic Nuclei. University Science Books, Mill Valley, CA

Pellegrini S., 2010, ApJ, 717, 640

Pogge R. W., Martini P., 2002, ApJ, 569, 624

Rand R. J., 1997, ApJ, 474, 129

Riffel R. A., Storchi-Bergmann T., 2011, MNRAS, 417, 2752

Rosado M., Gabbasov R. F., Repetto P., Fuentes-Carrera I., Amram P., Martos M., Hernandez O., 2013, AJ, 145, 135

Rosario D. J., Whittle M., Nelson C. H., Wilson A. S., 2010, MNRAS, 408, 565

Rossa J., Dettmar R.-J., 2003, A&A, 406, 493

Schnorr Müller A., Storchi-Bergmann T., Riffel R. A., Ferrari F., Steiner J. E., Axon D. J., Robinson A., 2011, MNRAS, 413, 149

Shlosman I., Begelman M. C., Frank J., 1990, Nat, 345, 679

Simões Lopes R. D., Storchi-Bergmann T., de Fátima Saraiva M., Martini P., 2007, ApJ, 655, 718

Skrutskie M. F. et al., 2006, AJ, 131, 1163

Storchi-Bergmann T., Winge C., Ward M. J., Wilson A. S., 1999, MNRAS, 304, 35

Storchi-Bergmann T., Dors O. L., Jr, Riffel R. A., Fathi K., Axon D. J., Robinson A., Marconi A., Östlin G., 2007, ApJ, 670, 959

Storchi-Bergmann T., Lopes R. D. S., McGregor P. J., Riffel R. A., Beck T., Martini P., 2010, MNRAS, 402, 819

Ulvestad J. S., Wilson A. S., 1983, ApJ, 264, L7

Valdez-Gutiérrez M., Rosado M., Puerari I., Georgiev L., Borissova J., Ambrocio-Cruz P., 2002, AJ, 124, 3157

Voigtländer P., Kamphuis P., Marcelin M., Bomans D. J., Dettmar R.-J., 2013, A&A, 554, A133

Wilson A. S., Baldwin J. A., 1985, ApJ, 289, 124

This paper has been typeset from a TEX/LATEX file prepared by the author.